HHS Public Access

Author manuscript

Nat Chem Biol. Author manuscript; available in PMC 2018 July 19.

Published in final edited form as:

Nat Chem Biol. 2018 January ; 14(1): 86–93. doi:10.1038/nchembio.2511.

Synthetic beta cells for fusion-mediated dynamic insulin secretion

Zhaowei Chen[1,2,4], **Jinqiang Wang**[1,2,4], **Wujin Sun**[1,2], **Edikan Archibong**[1], **Anna R Kahkoska**[3], **Xudong Zhang**[1,2], **Yue Lu**[1,2], **Frances S Ligler**[1], **John B Buse**[3], and **Zhen Gu**[1,2,3,*]

[1]Joint Department of Biomedical Engineering, University of North Carolina at Chapel Hill and North Carolina State University, Raleigh, North Carolina, USA

[2]Division of Pharmacoengineering and Molecular Pharmaceutics and Center for Nanotechnology in Drug Delivery, Eshelman School of Pharmacy, University of North Carolina at Chapel Hill, Chapel Hill, North Carolina, USA

[3]Department of Medicine, University of North Carolina School of Medicine, Chapel Hill, North Carolina, USA

Abstract

Generating artificial pancreatic beta cells by using synthetic materials to mimic glucose-responsive insulin secretion in a robust manner holds promise for improving clinical outcomes in people with diabetes. Here, we describe the construction of artificial beta cells (AβCs) with a multicompartmental ‘vesicles-in-vesicle’ superstructure equipped with a glucose-metabolism system and membrane-fusion machinery. Through a sequential cascade of glucose uptake, enzymatic oxidation and proton efflux, the AβCs can effectively distinguish between high and normal glucose levels. Under hyperglycemic conditions, high glucose uptake and oxidation generate a low pH (<5.6), which then induces steric deshielding of peptides tethered to the insulin-loaded inner small liposomal vesicles. The peptides on the small vesicles then form coiled coils with the complementary peptides anchored on the inner surfaces of large vesicles, thus bringing the membranes of the inner and outer vesicles together and triggering their fusion and insulin ‘exocytosis’

* zgu@email.unc.edu.

[4]These authors contributed equally to this work

Correspondence and requests for materials should be addressed to Z.G.

Author contributions

Z.C., F.S.L., J.B.B. and Z.G. designed the project; Z.C., J.W., W.S., E.A., X.Z. and Y.L. performed the experiments; Z.C., J.W., W.S., X.Z., E.A., Y.L. and Z.G. analyzed the data; Z.C., J.W., A.R.K., J.B.B., F.S.L. and Z.G. wrote the paper.

Competing financial interests

The authors declare no competing financial interests.

Additional information

Any supplementary information, chemical compound information and source data are available in the online version of the paper.

Publisher’s note: Springer Nature remains neutral with regard to jurisdictional claims in published maps and institutional affiliations.

Data availability. All data generated or analyzed during this study are included in this published article (and its supplementary information files) or are available from the authors upon reasonable request. A **Life Sciences Reporting Summary** for this paper is available.

The beta cells of the pancreas dynamically regulate insulin secretion, thereby maintaining blood glucose homeostasis. Destruction or dysfunction of these cells leads to type 1 and type 2 diabetes mellitus, a family of chronic diseases that currently affect over 415 million people worldwide[1–3]. Inadequate glucose control caused by loss of beta-cell function can lead to hyperglycemia, a condition directly implicated in the development of severe complications, including blindness, renal failure and cardiovascular disease[4]. However, the traditional intensive insulin therapy involving periodic injections imperfectly simulates the dynamics of beta cells and can cause hypoglycemia, which is associated with risks of behavioral and cognitive disturbance, brain damage or death[5–7]. To this end, cell therapy is gathering momentum as a promising strategy for restoring tight glycemic control while mitigating episodes of both hyper- and hypoglycemia in patients with diabetes[8–10]. However, this approach is limited by a shortage of donor islets and the requirement for immunosuppression after transplantation[11].

As an alternative to the use of living cells for therapeutic purposes, a variety of biomimetic assemblies have been proposed to recreate the key functions of cells[12,13]. Prominent examples of complex assemblies include cell-membrane-cloaked nanoparticles, deformable microgels or vesicles bearing integrated proteins for detoxification, vaccination, hemostasis and drug release[14–18]. All such assemblies can be viewed as single-compartment structures, and their interactions with biological entities are relatively passive compared with those exhibited by ‘living’ cells. Although multicompartmentalized assemblies have been created to reconstitute the hierarchical architecture of cells for delivering drug cocktails or conducting cascade reactions[19–24], replicating the ‘sense-reactive’ behaviors of natural cells still remains elusive. Indeed, a key challenge in the *de novo* design of synthetic therapeutic cells is to mimic the higher-order functions of their natural counterparts that can precisely sense the external environment, make internal decisions and trigger feedback[12,25], processes routinely used by pancreatic beta cells in response to changes in glycemic levels.

Like other biomolecule-secreting cells, beta cells export cellular cargos to the extracellular space through a vesicle transport system and a membrane-fusion process after external stimulation[26–28]. To mimic this biochemical cascade, using a vesicles-in-vesicle superstructure as a rational starting point, we designed and engineered a synthetic AβC (Fig. 1a and Supplementary Results, Supplementary Fig. 1). To our knowledge, this synthetic system is the first of its kind that can sense glucose levels and readily secrete insulin through vesicle-fusion-mediated behavior. The inner small liposomal vesicles (ISVs) are loaded with insulin to mimic the storage granules inside mature beta cells, and the outer large vesicle (OLV) mimics the plasma membrane. To endow the system with the capability to both sense glycemic levels and release insulin via fusing ISVs with OLVs, the hierarchical liposomal assembly is equipped with a glucose-relevant metabolic system and pH-controllable membrane-fusion machinery. Glucose is taken up by the anchored glucose transporter 2 (GLUT2) and is subsequently oxidized into gluconic acid by glucose oxidase (Fig. 1a). The released protons rapidly decrease the pH in the system. The net pH variation is balanced by efflux through the proton channel gramicidin A inserted in the OLV membrane, which allows for greater variation in the internal pH levels under hyperglycemic conditions. Subsequently, the low pH associated with high glucose concentrations triggers

dehybridization of the polyethylene glycol 5000–conjugated cytosine-rich DNA (PEG–CDNA) and the cholesterol-ended guanine-rich DNA (GDNA–CH) anchored on the ISVs, thereby sterically deshielding peptide K and making it available to form coiled coils with peptide $E^{29–37}$ on the inner surface of the OLV. The two peptides' 'zippering up' pulls the membranes of ISV and OLV tightly together and forces fusion, after which insulin is 'exocytosed'. When the glucose concentration declines to a normoglycemic range, glucose uptake decreases, and the inner pH level increases, thus allowing the ISVs to reanchor with PEG–CDNA and subsequently inhibit the fusion event. In this biomimetic manner, the AβCs can effectively respond to hyperglycemia and resume their basal low level of insulin release under resting conditions.

RESULTS

Construction of the AβCs

To implement the AβC design, insulin-loaded ISVs were first prepared via the classic lipid-film hydration method[38], in which 4 mol% PEG–CDNA/GDNA–CH (Supplementary Fig. 2) and 1 mol% peptide K were inserted into the membrane by *in situ* modification. Transmission electron microscopy (TEM) images indicated an average ISV diameter of 50 nm (Fig. 1b). Because of the conformational switch between double-stranded duplex DNA and intramolecular tetraplex structures at physiological pH and acidic pH[39,40] (pH <6.0; Supplementary Fig. 3), the PEG shield was able to reversibly attach to and disassociate from the ISVs, as evidenced by fluorescence resonance energy transfer (FRET) analysis (Supplementary Fig. 4). The peptide K and peptide E were each designed with three features: a transmembrane domain, a spacer and a recognition motif (Supplementary Fig. 5a), thus mimicking the SNARE membranefusion proteins[29–37]. As such, heterodimeric coiled coils driven by the electrostatic and hydrophobic interactions of the heptad repeats in the recognition region formed when peptide E and peptide K were mixed (Supplementary Fig. 5b). After insertion of the pH-responsive PEG shield in ISVs, an interaction between peptide E and peptide K was expected only in the unshielded state, on the basis of previous studies[33,34]. ISVs and glucose oxidase/catalase were encapsulated into OLVs decorated with 2 mol% peptide K by heating of interdigitated dipalmitoylphosphatidylcholine sheets above the gel–liquid phase-transition temperature[41] (Supplementary Fig. 6). Annealing of the interdigitated phospholipid sheets led to the formation of closed compartments with large size and high internal volume[41], thus simultaneously entrapping enzymes and ISVs. Catalase was added to decompose the undesired hydrogen peroxide and regenerate oxygen, thereby facilitating glucose oxidation (Supplementary Fig. 7). The resulting vesicles-in-vesicle superstructures with an overall size of ~1–5 μm were clearly observed in cryogenic scanning electron microscopy (cryo-SEM) images (Fig. 1c,d), cryogenic TEM images (Supplementary Fig. 8) and confocal microscopy video (Supplementary Video 1). The localization of glucose oxidase/catalase inside the cavities of OLVs was demonstrated by confocal laser microscopy imaging (CLSM; Fig. 1e). Next, GLUT2 (details of expression and purification in Supplementary Fig. 9a and Supplementary Note) was reconstituted into the OLV membrane through a freeze–thaw sonication method. The presence of GLUT2 on the OLV membrane was verified by western blotting (Fig. 1f; uncropped gel image in Supplementary Fig. 9b) and CLSM imaging (Fig. 1g). Finally, gramicidin A, a membrane-

spanning channel capable of conducting protons at very high flux rates[42], was inserted into the OLV membrane, as shown in the CLSM image, by incorporation of lysine-5-carboxyfluorescein-ended gramicidin (Fig. 1h).

Biochemical processes inside AβCs

To determine the glucose-sensing ability of the AβCs, we coupled the glucose-transport machinery to an interior enzymatic-oxidation scheme and a pH-sensitive dye (Supplementary Fig. 10). The biochemical process was monitored through fluorescence measurements (Fig. 2a,b and Supplementary Fig. 11a,b). At a fixed lipid/glucose transporter/glucose oxidase ratio, the inner pH level was dependent on the external glucose concentration as well as the amount of added gramicidin. At the same gramicidin level, the pH decrease was substantially faster at 400 mg/dL glucose (a level typical of hyperglycemia) than that at 100 mg/dL (a normoglycemic level). Moreover, similar pH variations but relatively slower kinetics were observed at levels reflecting modest hyperglycemia (300 and 200 mg/dL). The responsibility of the glucose transporter for glucose uptake was confirmed in control systems with no glucose transporter present as well as in the presence of the glucose-transport inhibitor cytochalasin B (Supplementary Fig. 12). Given that GLUT2 has a K_m of approximately 15–20 mM (ref. 43), and glucose oxidase has a K_m of approximately 33–100 mM, the difference in the pH decline may be attributed to the different glucose-transport rates associated with high and low glucose concentrations. When the glucose concentration was held constant, the inner pH was inversely correlated with the gramicidin content: as more gramicidin was inserted, protons were pumped out of the AβCs more rapidly. In control systems in which no gramicidin was inserted, the final pH at 100 mg/mL was similar to that under hyperglycemic conditions, although the pH decreased more slowly at 100 mg/dL thus indicating the necessity of gramicidin for tuning proton efflux to distinguish high and low glucose concentrations. The maximum pH change therefore relied on the overall kinetics of glucose uptake, glucose oxidation and proton efflux. For the following studies, we used AβCs with a gramicidin/lipid ratio of 1:2,000, which maintained pH <5.6 under hyperglycemic conditions and pH >6.5 under normoglycemic conditions. In this system, the pH inside the AβC switched in response to adjustments in glucose concentration (Fig. 2c and Supplementary Fig. 11c,d). Notably, the fast response in pH switching occurred because the diffusion of intermediates was minimized because all the biochemical processes were confined in a micrometer-scale space[44]. These unique properties enabled this artificial system to act similarly to natural beta cells in terms of precisely sensing graded glucose levels.

Next, we studied the ‘signal transduction’ inside AβCs, including the steric PEG deshielding and the subsequent peptide E–peptide K assembly. The disassociation of the PEG shield induced by glucose metabolism was confirmed via a FRET assay (Fig. 2d). The emission at 590 nm of the DNA donor tetramethylrhodamine on PEG– CDNA, which was initially quenched by the DNA acceptor IAbRQ on GDNA–CH gradually increased in 200–400 mg/dL glucose solutions, whereas almost no change was observed in 100 mg/dL glucose solution (Fig. 2e and Supplementary Fig. 13a). Owing to the slow kinetics for pH variation at glucose levels corresponding to modest hyperglycemia, the changes in PEG deshielding took a relatively longer time to initiate in 200 mg/dL and 300 mg/dL glucose solutions. A

control study of a pair of randomly sequenced complementary DNA strands generated no fluorescence recovery at either high or low concentrations over time (Supplementary Fig. 14). Furthermore, reversible association and disassociation of the PEG– CDNA was observed when the glucose concentrations were cyclically varied between high glucose levels and 100 mg/dL (Fig. 2f and Supplementary Fig. 13b,c), thus indicating that the conformational conversion at high glucose levels induced duplex dehybridization and hence detachment of the PEG shield.

Next, expecting that the signals of other peptides or proteins would preclude the use of CD techniques, we used FRET to study the pairing of peptide K on ISVs with peptide E on OLVs (Fig. 2g). The fluorescence of nitrobenzofuran on the peptide donor peptide K was readily quenched by the peptide acceptor tetramethylrhodamine on peptide E under high glucose concentrations (Fig. 2h and Supplementary Fig. 15a), and a stepwise decrease in peptide-donor fluorescence was observed when the glucose concentration was alternated between high glucose levels and 100 mg/dL (Fig. 2i and Supplementary Fig. 15b,c). The lag at the beginning of each switch was due to the inner pH variation and the time required for the PEG-shield attachment/detachment to reach equilibrium; this lag was longer in glucose solutions reflecting modest hyperglycemia than after switching to the high glucose concentrations. Critically, no peptide interactions were detected at low glucose levels or in control groups in which non-pH-responsive DNA was used (Supplementary Fig. 16), indicating the direct dependence of peptide assembly on the dissociation of the PEG shield from ISVs, in which protons generated by glucose (signal) metabolism act as the signal mediator, and the sequence-specific DNA strands act as the signal effector, thus allowing the signal transduction inside AβC to induce PEG deshielding and subsequently activate peptide assembly.

Membrane fusion of ISVs with OLVs

After a clear ‘signaling pathway’ was established, we next sought to substantiate the membrane fusion of the ISVs with OLVs which was driven by the interaction of peptide E and peptide K. By simultaneously incorporating lipids labeled with the lipid donor nitrobenzofuran and the lipid acceptor lissamine rhodamine B into the ISV, we studied the efficiency of lipid mixing at different glucose concentrations, using a standard dequenching assay (Fig. 3a). At high glucose concentrations, a continuous increase in lipid-donor emission around 536 nm was observed, a result indicative of dilution of the lipid-donor and lipid-acceptor dyes induced by membrane fusion (Fig. 3b and Supplementary Fig. 17a). In addition, as seen in the CLSM image (Fig. 3c), the green fluorescence of the lipid donor and the red fluorescence of the lipid acceptor gradually appeared and increased on the surfaces of AβCs in response to hyperglycemic conditions, and the fluorescence inside the AβCs gradually decreased, thus substantiating the merger of the ISV with the OLV. No obvious variations in lipid-donor fluorescence were observed under normoglycemic conditions (Fig. 3d). In further control experiments, no recovery in lipid-donor fluorescence was detected when either peptide E or peptide K was omitted (Supplementary Fig. 18). Because peptide E and peptide K have been reported to be the minimal machinery that can mimic SNARE proteins for controlling membrane fusion[31,32], these results therefore implied that peptide

assembly tuned by glucose signal transduction brought the ISV and OLV close together and transmitted the forces promoting their fusion.

In natural beta cells, vesicles can be trafficked to the periphery of the cell membrane with the assistance of the cytoskeleton[45], thus leading to a sustainable fusion process. In the absence of machinery mimicking the cytoskeleton, ISVs moved randomly by Brownian motion within the AβCs, as shown in the CLSM images (Fig. 3c,d and Supplementary Video 1). Both the peptide assembly and the effective contact between the randomly diffused ISVs and the OLV contribute to the observed fusion processes within AβCs[46], thus making the fusion process sustainable for several hours. In addition, cyclic switching of the glucose concentrations between hyperglycemic and normoglycemic levels resulted in stepwise increases in nitrobenzofuran fluorescence (Fig. 3e and Supplementary Fig. 17b,c). Thus, on the basis of the glucose-sensing ability of AβCs and the reversible attachment of the PEG shield on ISVs, this new glucose-responsive mechanism promotes fusion under hyperglycemic conditions and reshields the ISVs, thereby minimizing fusion under normoglycemic conditions for numerous cycles.

To exclude the possibility that the fusion process terminated at the stage of hemifusion[30–32], we further studied whether the inner lipid layers of ISVs effectively mixed with the outer lipid layer of OLVs by bleaching the lipid-donor fluorophores on the outside of the ISVs with sodium dithionite (Supplementary Fig. 19a). An increase in lipid-donor fluorescence was detected at 400 mg/dL glucose (Supplementary Fig. 19b). Because the FRET effect required the lipid-donor fluorophores inside the ISVs, complete merger of both the inner and outer lipid leaflets of the membranes of the ISVs and OLV occurred during fusion. Such full fusion of ISVs with OLVs is critical for the release of ISV cargoes outside the OLV in a manner that mimics cellular exocytosis.

In vitro dynamic insulin ‘secretion’ from AβCs

In accumulated-insulin-release studies, a remarkably rapid insulin release was detected at glucose levels reflecting hyperglycemia, whereas minimal release was observed at levels reflecting normoglycemia or in glucose-free buffer solution over 15 h (Fig. 4a and Supplementary Figs. 20 and 21a). Notably, the fast responsiveness of AβCs to 400 mg/dL glucose, as compared with the responsiveness of more conventional systems dependent on glucose oxidase–mediated pH decreases, resulted from the well-organized spatial confinement of all relevant biochemical processes. This compartmentalization was similar to that in natural cells and also decreased the interference from the buffered environment[11,47]. Furthermore, the slower insulin release at modest glucose levels contributes to the dynamic response of AβCs toward different blood glucose levels. When insulin was conjugated with fluorescein isothiocyanate, CLSM imaging showed more homogeneously distributed green fluorescence for AβCs in high-glucose solution, whereas clustered green signals remained in 100 mg/mL glucose after incubation for 6 h (Fig. 4b and Supplementary Fig. 21b), thus substantiating the release of insulin under hyperglycemic conditions. In control groups in which AβCs lacked either glucose-sensing machinery or membrane-fusion peptides, we observed slow and indistinguishable insulin-release kinetics at all glucose levels (Supplementary Fig. 22a,b). Furthermore, when the glucose concentrations were cyclically

alternated between 400 mg/dL and 100 mg/dL every 1 h for several repetitions, a pulsatile release profile was measured for AβCs, with a maximum eight-fold difference in insulin release (Fig. 4c). The low levels of released insulin detected after switching of the glucose concentration to normoglycemic levels was due to the lag across glucose metabolism, pH variation and membrane fusion. However, no such oscillations were found for the control AβCs (Supplementary Fig. 22c,d). In addition, no obvious insulin release was observed under mildly acidic pH levels (Supplementary Fig. 23), thus suggesting that nonspecific activation of AβCs would not occur in diabetic mice with diabetic ketoacidosis, which typically leads to plasma pH levels below 7.3 (ref. 48). These results illustrated that the oscillations in the glucose pathway and membrane fusion (demonstrated above) of AβCs effectively contributed to the oscillatory feature of insulin release, thus closely mimicking the dynamic secretion features of natural beta cells.

In vivo type 1 diabetes treatment

We further tested the ability of AβCs to regulate blood glucose levels *in vivo* in a streptozotocin (STZ)-induced type 1 diabetic mouse model. Before *in vivo* studies, the retention of the secondary structure and the bioactivity of the insulin released from AβCs was verified (Supplementary Figs. 24 and 25). The AβCs were 'transplanted' into subcutaneous tissues by injection of a Pluronic F-127 (PF127) solution (40 wt%) containing homogeneously distributed AβCs, a delivery method relying on PF127's biodegradability and ability to quickly form a stable hydrogel at body temperature[49] (Supplementary Fig. 26). The distribution and integrity of AβCs inside the hydrogel were clearly observed under cryo-SEM imaging (Supplementary Fig. 27). In control groups, AβCs lacking insulin ($A\beta C_{(no\ insulin)}$), lacking membrane-fusion peptides ($A\beta C_{(no\ PE/PK)}$) or lacking glucose-sensing machinery ($A\beta C_{(no\ GSM)}$) were also injected. The blood glucose in the mice treated with AβCs quickly declined from hyperglycemic to normoglycemic levels within 1 h, and subsequently the blood glucose levels remained normoglycemic for up to 5 d (Fig. 4d,e). In contrast, mice treated with $A\beta C_{(no\ insulin)}$ showed elevated blood glucose levels, thus excluding the possibility of a decrease in blood glucose levels induced by catalytic consumption. For groups treated with control AβCs, elevated blood glucose levels were also observed because of the lack of self-regulated glucose-sensing or membrane-fusion abilities. Correspondingly, plasma insulin levels in mice treated with AβCs remained detectable over the time course, whereas little or no plasma insulin was detected in the plasma of control mice (Fig. 4f). Intraperitoneal glucose tolerance tests were performed to further test the *in vivo* glucose-responsive ability of AβCs at 24, 36 and 48 h after 'transplantation' (Fig. 4g). At each time point, after showing a spike in blood glucose levels, mice that had received AβCs showed restoration of prechallenge blood glucose levels at a rate comparable to that in healthy mice. Similar results were still observed on the fifth day after injection (Supplementary Fig. 28). However, this phenomenon was not observed for mice treated with control artificial cells in the same test (Supplementary Fig. 29). This *in vivo* responsive ability of the designed AβCs was further demonstrated by detection of the protein release in wild-type mice that were treated with AβCs loaded with human serum albumin 1.5 h after administration of glucose (Supplementary Fig. 30).

Importantly, AβCs$_{(no\ insulin)}$ were not associated with obvious cytotoxicity at any of the concentrations studied (Supplementary Fig. 31). Finally, the injected formulation including PF127 was completely degraded by 4 weeks after administration, and no noticeable inflammatory regions or fibrotic encapsulations were observed (Supplementary Fig. 32). Moreover, no obvious differences in body-weight changes were observed between treated groups and the PBS-injected control group (Supplementary Fig. 33). In addition, the levels of inflammatory factors such as TNF, IL-1β and IL-6 in the treated groups were similar to those in the control groups (Supplementary Fig. 34).

DISCUSSION

In conclusion, we demonstrated synthetic AβCs that recapitulate the key functions of beta cells, including sensing glucose levels, internally transducing signals and dynamically secreting insulin via vesicle fusion. Several differences exist between our AβCs and natural beta cells. The natural beta cells are electrically excitable and leverage variations in membrane potential, thereby coupling fluctuations in blood glucose levels to stimulation or inhibition of insulin secretion[1]. In contrast, the glucose sensing and stimulated insulin exocytosis inside AβCs are simplified into pH-tuned dynamic processes within confined microenvironments. Furthermore, natural beta cells secrete insulin via a biphasic process (involving a rapid first phase and prolonged second phase) that maintains a baseline level of insulin release at all times. In AβCs, the random collision of the insulin-containing ISVs with the outer membrane and subsequent induction of peptide interactions allowed a low level of the fusion process to be sustained for several hours. Moreover, the AβCs did not show the transient burst of insulin release that has often been reported in conventional pH-responsive materials, thus potentially conferring protection against lifethreatening insulin-induced hypoglycemia. Moreover, on the basis of the reversible nature of pH-tuned PEG attachment and detachment, pulsatile insulin release in response to graded glucose concentrations can run for many cycles, thereby potentially being able to withstand the blood glucose fluctuations that are prominent in even well-controlled type 1 and type 2 diabetes. One of the greatest advantages of the AβCs is that they can be ‘transplanted’ directly within an injectable gel or potentially delivered through transcutaneous microneedle patches to restore blood glucose homeostasis[2], thereby avoiding use of the immunosuppressive drugs required for transplantation of live cells. Our demonstration suggests that automated dynamic control of blood glucose concentrations to levels within a near-normal range would be feasible with synthetic artificial cells.

Nonetheless, opportunity exists in further improving the performance of AβCs. For large-scale bioprocessing, the design and synthesis of AβCs should be simplified without compromising the key functions mimicking natural beta cells. Another important aspect of the current design that needs improvement is the ability to provide continued insulin release for sustained therapy in a manner similar to that of natural beta cells or designer cells[8,50]; however, equipping synthetic cells with insulin- or other protein-replenishing machinery remains a major challenge. Moreover, issues regarding the accuracy of ‘transplantation’ and the extent of the engrafted AβCs should be addressed to optimize the therapeutic performance. Although many gaps remain between biomimetic assemblies and natural cells, the described design principles lay a groundwork for developing next-generation artificial

cells with the goal of achieving long-term replacement therapy to correct for cell-function deficiencies[51,52].

ONLINE METHODS

Materials and general methods

Materials—All lipids including egg phosphatidylcholine (EPC), 1,2-dioleoyl-*sn*-glycero-3-phosphoethanolamine (DOPE), dipalmitoylphosphatidylcholine (DPPC), 1,2-dioleoyl-*sn*-glycero-3-phospoethanolamine- *N*-(7-nitro-2-1,3-benzoxadiazol-4-yl) (ammonium salt) and 1,2-dioleoyl-*sn*-glycero-3-phosphatidylethanolamine-lissamine–rhodamine B were purchased from Avanti Polar Lipids. All peptides were synthesized by Biochem Co. All DNAs were purchased from DNA Technologies. Cholesterol, glucose oxidase, catalase, gramicidin A, methoxypolyethylene glycol maleimide (mPEG-Mal, MW 5,000), PMSF, *n*-dodecyl β-D-maltoside (DDM) and 8-hydroxypyrene-1, 3, 6-trisulphonic acid trisodium salt (HPTS) were purchased from Sigma-Aldrich. Human recombinant insulin was purchased from Life Technologies. Anti-GLUT2 antibody was purchased from Abcam (cat. no. ab54460).

Instrumentation—CD spectra were recorded with a Jasco J-815 spectropolarimeter while the sample cell was flushed with nitrogen. TEM images were acquired with a JEOL 2000FX scanning transmission electron microscope at 200 kV. Fluorescence measurements were carried out with a FLS980 fluorescence spectrophotometer (Edinburgh Instruments). ELISAs, insulin detection and cell viability analysis were performed with an Infinite 200 PRO multimode plate reader (Tecan). Confocal microscopy images were obtained with a Zeiss LSM 710 confocal microscope (Carl Zeiss), and the samples were visualized with the same acquisition settings and analyzed in Zen 2011 software (Carl Zeiss). Confocal microscopy movies were recorded with a Zeiss LSM 880 Airyscan microscope. Cryogenic TEM images were acquired with the help of the ICBR Electron Microscopy Core at the University of Florida. The blood glucose levels in mice were monitored with a Clarity GL2Plus glucose meter (Clarity Diagnostics). Cryo-SEM images were obtained with a JEOL 7600F microscope equipped with a Gatan Alto system. After cryofracture of the larger liposomes, the samples were then sublimated at −95 °C for 5 min under 10^{-6}-mbar vacuum. This step was used to reveal the internal fine structure by sublimating the ice crystals. The darker background outside the larger liposomes was ice. From the differences in brightness, we were able to distinguish the ice and the small-liposome nanoparticles.

Statistical analysis—Biological replicates were used in all experiments. one-way analysis of variance (ANOVA) with Tukey *post hoc* tests was used to determine statistical significance between different groups. A P value <0.05 was considered to be statistically significant. All statistical analyses were performed in Origin 8.5. No statistical methods were used to predetermine the sample size of the experiments unless otherwise stated.

Design and synthesis of AβCs

Synthesis of PEG shield—3′-thiolated cytosine-rich DNA (CDNA) and mPEG-Mal solution at a DNA/mPEG-Mal molar ratio of 1:5 were mixed in HEPES buffer (1 mM, pH

7.5) and incubated for 4 h. The conjugation of PEG with CDNA was verified by agarose gel (1%) electrophoresis (Supplementary Fig. 2a), in which PEG–CDNA showed a much slower mobility than did CDNA. The cholesterol-ended guanine-rich DNA (GDNA– CH) was then mixed with PEG–CDNA to form a duplex-DNA-bridged PEG shield (PEG–CDNA/GDNA–CH), which was inserted into liposome membranes. The fluorescently labeled DNA and non-pH-responsive DNA-bridged PEG shield were prepared through the same process. The DNA-bridged PEG shields were lyophilized before preparation of liposomes. The sequences of all DNAs are shown in Supplementary Table 1. The conformational switch of the PEG–CDNA/GDNA–CH and non-pH-responsive DNA-bridged PEG shield at different pH values was studied by CD spectroscopy (Supplementary Fig. 3). From the CD spectra, no conformational variation was observed for the control DNA; however, for PEG–CDNA/GDNA–CH, the characteristic peak of DNA tetraplex at around 290 nm increased as the pH decreased. The CD spectra of PEG–CDNA/GDNA–CH indicated that the PEG–CDNA/GDNA–CH mainly existed as duplexes at and above pH 6.5, whereas the PEG–CDNA/GDNA–CH disassociated into tetraplexes at and below pH 5.5.

Preparation of insulin-loaded fusogenic ISVs labeled with peptide K and PEG shield—Lipid stock solution was prepared in chloroform with the composition of EPC/DOPE/CH 2.5:2.5:1 (w/w/w). Peptide K (50 μM) and PEG shield (50 μM) stock solutions were prepared in chloroform/methanol 1:1 (v/v) and methanol, respectively. Then a solution of lipids, peptide K and PEG shield was prepared with a final molar ratio of 95:1:4 and added to a round-bottom flask. Afterward, the solvent was evaporated with a rotary vacuum evaporator to yield lipid film, which was then dried under vacuum overnight. Next, insulin was dissolved in 4 mL HEPES buffer (5 mM and 150 mM NaCl, pH 7.4) and added to rehydrate the lipid film with gentle vortexing. A total of 50 mg of insulin was used for each 100 mg of lipid. The resulting suspension was sonicated with a probe sonicator for 5 min with a power of 100 W and a time interval of 1s/1s to obtain a milky suspension. Afterward, the suspension was extruded ten times through polycarbonate membranes with a pore size of 100 nm, by using an Avanti Mini Extruder. Free insulin was removed by centrifugation at 20,000 r.p.m. for 60 min at 4 °C, and the liposomes were washed twice. To the sedimented liposomes, 4 mL HEPES buffer was added to yield the final insulin-loaded ISVs. The loading efficiency of insulin was calculated as the ratio of the concentrations of the liposome-associated insulin to the initially added insulin and was determined by a Coomassie Plus protein assay to be approximately 36.4%. ISVs without insulin or peptide K were prepared in the same manner and used in control experiments.

Preparation of interdigitated DPPC-bilayer sheets—To prepare interdigitated bilayer sheets[41,53,54], DPPC dissolved in chloroform and peptide E dissolved in chloroform/methanol 1:1 (v/v) at a molar ratio of 98:2 were added to a round-bottom flask. After the solution was evaporated to form thin lipid films, HEPES buffer was added, and the film was hydrated at 60 °C. The final lipid concentration was 50 mg/mL. Afterward, the suspension was sonicated at 60 °C for 5 min with a power of 100 W and a time interval of 1s/1s to obtain a milky suspension. Then the solution was extruded ten times sequentially through syringe filters with pore sizes of 200 and 100 nm at 60 °C to obtain liposomes with sizes less than 100 nm (Supplementary Fig. 6a,b). Afterward, interdigitated sheets were formed by

dropwise addition of ethanol to 0.5 mL of the DPPC liposomes; the final concentration of ethanol was typically 3 M. The solution was allowed to sit for 2 h to ensure complete interdigitation. The resulting sheets were then washed three times through addition of 3 mL HEPES buffer to remove excess ethanol, subsequent centrifugation at 5,000 r.p.m. and removal of supernatant. The obtained sheets were characterized by cryo-SEM (Supplementary Fig. 6c) and TEM (Supplementary Fig. 6d).

Building AßCs—To encapsulate ISVs inside OLVs, 0.5 mL of the ISVs prepared as above, 6 mg glucose oxidase and 1.5 mg catalase were added to one batch of the DPPC sheets prepared as above. Then the mixture was heated at 45 °C (above the main transition temperature of DPPC) for 20 min under gentle stirring to drive the sheets to close around ISVs and glucose oxidase/catalase to form the vesicles-in-vesicle superstructures (ISVs@OLV)[41,53,54]. The free ISVs and glucose oxidase/catalase were removed by centrifugation at ~2,000 r.p.m. and were washed twice. All the supernatant was collected and ultracentrifuged to measure the loading efficiency of ISVs and glucose oxidase/catalase. The amount of ISVs encapsulated inside OLVs was determined indirectly on the basis of the amount of insulin in the free ISV. Approximately 52.8% of the ISVs were encapsulated. The unencapsulated glucose oxidase/catalase was detected by Bradford assays to measure the protein amounts in the supernatant after ultracentrifugation. Approximately 45.2% of glucose oxidase/catalase was encapsulated. Then GLUT2 (expression and purification methods described below) was reconstituted onto the OLV according to a previously reported method[55]. Approximately 1 mg of GLUT2 was mixed with one-fifth of the centrifuged ISVs@OLV in 0.5 mL HEPES buffer. After being mixed to homogeneity, the suspension in a tube was quickly frozen in liquid nitrogen for 5 min and was subsequently sonicated for 20 or 30 s in a bath sonicator. The suspension was centrifuged at ~2,000 r.p.m. and washed twice to remove free GLUT2. The reconstitution efficiency of GLUT2 was determined to be 82% with GLUT2 ELISA kits. Finally, the proton channel gramicidin A in different ratios to DPPC in DMSO solution was added to the suspension of GLUT2-recontituted ISVs@OLV used for the following experiments.

GLUT2 expression and purification—The cDNA encoding mouse GLUT2 (Origene, GenBank NM_031197) was amplified and cloned into the BamHI and HindIII sites of pET-28a (Novagen; full plasmid sequence in Supplementary Note). The constructed plasmid was transfected into *Escherichia coli* Rosetta (DE3) pLysS cells for GLUT2 expression. The *E. coli* cells were cultured in lysogeny broth supplemented with kanamycin and chloromycetin, and protein expression was induced with 0.5 mM IPTG. The cells were collected by centrifugation and resuspended in buffer A (20 mM Tris-HCl, pH 8.0, 0.15 M NaCl, 10 mM imidazole, 1 mM PMSF, 5% glycerol, 0.4 mg/mL DNase I, 2% DDM and 0.5 mg/mL lysozyme). The suspension was incubated at 25 °C for 0.5 h and kept on ice for another 0.5 h. After brief sonication, cell debris was removed by centrifugation (20,000*g*, 10 min). The clear supernatant was added to a column filled with Ni–NTA resin (Qiagen). After the column was washed with buffer B (20 mM Tris-HCl, pH 8.0, 25 mM imidazole, 5% glycerol, 0.15 M NaCl and 0.05% DDM), GLUT2 was eluted with buffer C (20 mM Tris-HCl, pH 8.0, 0.15 M NaCl, 500 mM imidazole, 5% glycerol and 0.05% DDM). The purified

GLUT2 was quantified with Bradford assays (Bio-Rad), and the purity was analyzed through SDS–PAGE (Supplementary Fig. 9).

Biochemical processes inside AβCs

Glucose sensing and metabolism by AβCs—The fluorescence intensities of HPTS (514-nm emission; 406-nm (I_{406}) and 460-nm (I_{460}) excitation) were strongly dependent on the degree of ionization of the 8-hydroxyl group (pK_a = 7.2) and hence on the pH of the medium. The I_{406} and I_{460} increased linearly with increasing HPTS concentration up to 2 μM (refs. 42,56). The titration curve of HPTS (0.5 μM) at different pH levels (5 mM HEPES buffer and 100 mM NaCl) was measured as shown in Supplementary Figure 10a. For glucose sensing, HPTS was loaded with ISV/GOx/CAT inside the OLV simultaneously during the encapsulation process and was used as the pH probe to measure the pH variation inside AβCs, as induced by glucose uptake, glucose oxidation and proton efflux. To maintain a physiologically relevant and constant external glucose concentration, 100 μL HEPES buffer containing HPTS-loaded AβCs and glucose at different concentrations was added into the cup of a Slide-A-Lyzer MINI Dialysis Device (2K), and 1.5 mL isotonic solution containing the same concentration of glucose was added to the tube. The MINI Dialysis Device was then gently shaken at 37 °C. At predetermined time intervals, 30 μL of the solution in the cup was removed, and the fluorescence intensities at 510 nm with 400-nm and 450-nm excitation were detected. The pH values inside AβC were calculated with the titration curve shown in Supplementary Figure 10b. After measurement, the solution was returned back to the cup of the MINI Dialysis Device. For the glucose-concentration-switching experiments, AβCs were first incubated in high-glucose solutions to reach equilibrium, and then AβCs' ability to sense changes in glucose levels was assessed. After each switch, the inner pH was measured until equilibrium was reached, and then the AβCs were centrifuged and resuspended in another glucose solution. The cycles were repeated several times.

Signal transduction inside AβCs—We first studied the PEG-shield attachment onto and dissociation from the ISV surface, as triggered by the pH variation induced by glucose metabolism. Because our AβCs contained proteins or peptides that also had CD signals, we alternatively applied the FRET method to monitor this process by using fluorescent dye (tetramethylrhodamine DNA donor) to label CDNA and quencher (IAbRQ DNA acceptor) to label GDNA (Supplementary Table 1). In these experiments, similarly to the glucose sensing experiments, the AβC solution was collected at predetermined time intervals or cycle runs, and the fluorescence variation of the DNA donor at different glucose concentrations was determined. To study the PEG-shedding-facilitated peptide assembly of peptide E on ISV with peptide K on the inner surfaces of OLVs, the FRET method was also used with lysine-nitrobenzofuran (peptide donor)-modified peptide K and lysine-5-carboxytetramethylrhodamine (peptide acceptor)-labeled peptide E. The interaction of the peptide was determined on the basis of the quenching efficiency of the peptide donor by the peptide acceptor at different glucose concentrations.

Membrane fusion

The fusion of ISVs with OLVs in response to different glucose concentrations was studied with a dequenching method based on FRET. Fluorescence experiments were carried out with ISVs colabeled with the FRET pair 1,2-dioleoyl-*sn*-glycero-3-phospoethanolamine-*N*-(7-nitro-2-1,3-benzoxadiazol- 4-yl) (ammonium salt) (lipid-donor, 0.5 mol%), and 1,2-dioleoyl-*sn*glycero- 3-phosphatidylethanolamine-lissamine–rhodamine B (lipid acceptor, 0.5 mol%). After incubation of AβC in different glucose solutions, the recovery of lipid-donor fluorescence was detected at different time intervals. The change in lipid-donor fluorescence intensity was plotted as:

$$F(\%) = 100 \times (F_t - F_0)/(F_{\max} - F_0)$$

where F_0 is the lipid-donor fluorescence intensity at $t = 0$ before addition to glucose solution, F_t is the lipid-donor fluorescence intensity measured at time t, and $F_{\max}$ is the lipid-donor fluorescence intensity after disruption of the AβC in 1% (w/v) Triton X-100.

In addition, the fusion process was monitored through confocal laser microscopy imaging (Zeiss LSM 710). Images were obtained at different times after incubation in glucose solution.

For experiments demonstrating that no hemisfusion stage existed, the outer fluorescence of ISVs colabeled with lipid donor and lipid acceptor was bleached by incubation with sodium dithionate[31] (Supplementary Fig. 19). The excess sodium dithionate was removed by centrifugation at 20,000 r.p.m. Then the fusion of the ISV inner membrane with the OSV outer membrane was detected through an identical dequenching assay.

In vitro dynamic insulin secretion from AβCs

100 μL AβC mixed with glucose solutions at different concentrations was added into the cup of a Slide- A-Lyzer MINI Dialysis Device (2K), and 1.5 mL isotonic solution containing the same concentration of glucose was added to the tube. Then the MINI Dialysis Device was gently shaken at 37 °C. At the indicated time points, 15 μL of the solution in the cup was removed and centrifuged at 6,000 r.p.m. for 1 min. Then certain volumes of the supernatant were removed, and insulin was measured with a Coomassie Plus protein assay. The insulin concentration was calculated with a standard curve (Supplementary Fig. 21). For concentrated samples, dilution to the range of the standard curve was necessary. The remaining mixture was adjusted to its previous volume with fresh glucose solution and re-added to the cup. For pulsatile release studies, the AβCs were first incubated within 400 ml/dL solution for 60 min and then spun down by centrifugation and washed once with HEPES buffer. The AβCs were then resuspended in 100 mg/dL glucose solution for another 60 min. The cycles were repeated numerous times. Similarly, insulin concentration was determined with a Coomassie Plus protein assay.

In vivo diabetes treatment

Animals—Animal experiments were performed according to an animal protocol approved by the Institutional Animal Care and Use Committee at the University of North Carolina at

Chapel Hill and North Carolina State University. STZ-induced C57BL/6 type 1 diabetic mice were purchased from the Jackson Laboratory. Experimental-group sizes were approved by the regulatory authorities for animal welfare after being defined to balance statistical power, feasibility and ethical aspects. For all the animal studies, mice were randomly allocated to each group. The researchers were not blinded to group allocation during the animal studies, as required by the experimental designs.

Diabetes treatment—The *in vivo* efficacy of AβCs was investigated in STZ-induced adult diabetic mice (male, age 8 weeks). At 2 d before injection of the AβCs, the blood glucose levels of the mice were monitored with a Clarity GL2Plus glucose meter (Clarity Diagnostics) in ~3 μL blood collected from the tail vein, and all mice were fasted overnight before testing. To mimic beta-cell transplantation, AβCs were suspended in 40% PF127 solution for thermogel formation and subcutaneously injected into the dorsum in diabetic mice (Supplementary Fig. 26). A total of 300 μL of AβC/PF127 in PBS buffer or other control mixture was subcutaneously injected into the dorsum in mice given an insulin dose of 50 mg/kg after isoflurane anesthesia. Five mice in a stable hyperglycemic state were chosen from each group and subjected to administration of $A\beta C_{(no\ insulin)}$ or control AβCs that lacked either glucose-sensing machinery or membrane-fusion peptides ($A\beta C_{(no\ GSM)}$ and $A\beta C_{(no\ PE/PK)}$). The blood glucose levels of the mice were monitored over time (every 15 min or 1 h for the first 12 h after administration and once per day in the subsequent days) until stable hyperglycemia had been reached. To confirm the bioactivity of the released insulin, insulin solution (20 μg of native insulin or insulin released from AβCs at 400 mg/dL glucose for 6 h) was subcutaneously injected into the dorsum in diabetic mice. To measure the plasma insulin levels *in vivo*, 25-μL blood samples were collected from the tail veins of mice at the indicated time points. The plasma was isolated and stored at −20 °C until being assayed. The plasma insulin concentrations were measured with a Human Insulin ELISA kit according to the manufacturer's protocol (Calbiotech). A series of glucose-tolerance tests were conducted at 24, 36 and 48 h after treatment to confirm effective release of insulin from the AβCs in response to the glucose challenge. Briefly, glucose solution in PBS was intraperitoneally injected into all mice at a dose of 1 g kg^{-1}. The blood glucose levels were closely monitored for 120 min after injection. Glucose tolerance tests on healthy mice were used as controls.

Cell culture—HeLa cells were obtained from the Tissue Culture Facility of the UNC Lineberger Comprehensive Cancer Center. The cells were cultured in Dulbecco's Modified Eagle's Medium (Gibco, Invitrogen) with 10% (v/v) FBS (Invitrogen), 100 U ml^{-1} penicillin (Invitrogen) and 100 mg ml^{-1} streptomycin (Invitrogen) in an incubator (Thermo Scientific) at 37 °C under an atmosphere of 5% CO_2 and 90% relative humidity. Cells were tested every three months for potential mycoplasma contamination. Reauthentication of cells was not performed after receipt.

Biocompatibility evaluation—The cytotoxicity of $A\beta C_{(no\ insulin)}$ was examined in HeLa cells through a 3-(4,5)-dimethylthiahiazo(-z-y1)-3,5-di-phenytetrazoliumromide (MTT) assay. Briefly, HeLa cells were seeded at a density of 5,000 cells per well (200 μL total volume per well) in 96-well plates. After 24 h, $A\beta C_{(no\ insulin)}$ at the indicated concentrations

was added, and cells were further incubated for 24 h. Thiazolyl blue solution (5 mg mL^{-1}) was added into the wells (final concentration 0.5 mg mL^{-1}) and incubated with the cells for 4 h. After removal of the culture medium, the purple formazan crystals were dissolved in 200 μL of DMSO. The absorbance at 570 nm, which is directly proportional to the viable cell number, was measured on an Infinite 200 PRO multimode plate reader (Tecan).

To evaluate the *in vivo* biocompatibility of AβC, 4 weeks after injection of AβC/PF127, the diabetic mice were euthanized via CO_2 asphyxiation, and the injected materials and surrounding tissues were excised. The tissues were then fixed in 10% formalin, embedded in paraffin, cut into 5-μm sections and stained with hematoxylin and eosin for histological analysis. At that time, the body weights of the diabetic mice in each group were recorded. Moreover, for immunological analysis, representative inflammatory factors, such as TNF, IL-1β and IL-6, in the sera of mice from each group were measured by ELISA (eBioscience, Thermo Fisher Scientific) according to the manufacturer's instructions.

Supplementary Material

Refer to Web version on PubMed Central for supplementary material.

Acknowledgments

This work was supported by grants from the American Diabetes Association (grant no. 1-15-ACE-21 to Z.G.), Alfred P. Sloan Foundation (Sloan Research Fellowship to Z.G.), National Science Foundation (grant no. 1708620 to Z.G.) and NC TraCS, NIH's Clinical and Translational Science Award (CTSA, grant no. 1UL1TR001111) at UNC-CH. This work was performed in part at the Analytical Instrumentation Facility (AIF) at North Carolina State University, which is supported by the State of North Carolina and the National Science Foundation (grant no. 1542015). The AIF is a member of the North Carolina Research Triangle Nanotechnology Network (RTNN), a site in the National Nanotechnology Coordinated Infrastructure (NNCI). The authors also thank P. Chipman and R. Alvarado at the University of Florida's ICBR center.

References

1. Rorsman P, Braun M. Regulation of insulin secretion in human pancreatic islets. Annu Rev Physiol. 2013; 75:155–179. [PubMed: 22974438]
2. Yu J, et al. Microneedle-array patches loaded with hypoxia-sensitive vesicles provide fast glucose-responsive insulin delivery. Proc Natl Acad Sci USA. 2015; 112:8260–8265. [PubMed: 26100900]
3. Ohkubo Y, et al. Intensive insulin therapy prevents the progression of diabetic microvascular complications in Japanese patients with non-insulin-dependent diabetes mellitus: a randomized prospective 6-year study. Diabetes Res Clin Pract. 1995; 28:103–117. [PubMed: 7587918]
4. Nathan DM. Long-term complications of diabetes mellitus. N Engl J Med. 1993; 328:1676–1685. [PubMed: 8487827]
5. Nathan DM. The diabetes control and complications trial/epidemiology of diabetes interventions and complications study at 30 years: overview. Diabetes Care. 2014; 37:9–16. [PubMed: 24356592]
6. Nathan DM, et al. The effect of intensive treatment of diabetes on the development and progression of long-term complications in insulin-dependent diabetes mellitus. N Engl J Med. 1993; 329:977–986. [PubMed: 8366922]
7. Orchard TJ, et al. Association between 7 years of intensive treatment of type 1 diabetes and long-term mortality. J Am Med Assoc. 2015; 313:45–53.
8. Xie M, et al. β-cell-mimetic designer cells provide closed-loop glycemic control. Science. 2016; 354:1296–1301. [PubMed: 27940875]
9. Pepper AR, et al. A prevascularized subcutaneous device-less site for islet and cellular transplantation. Nat Biotechnol. 2015; 33:518–523. [PubMed: 25893782]

10. Vegas AJ, et al. Long-term glycemic control using polymer-encapsulated human stem cell-derived beta cells in immune-competent mice. Nat Med. 2016; 22:306–311. [PubMed: 26808346]
11. Veiseh O, Tang BC, Whitehead KA, Anderson DG, Langer R. Managing diabetes with nanomedicine: challenges and opportunities. Nat Rev Drug Discov. 2015; 14:45–57. [PubMed: 25430866]
12. Zhang Y, Ruder WC, LeDuc PR. Artificial cells: building bioinspired systems using small-scale biology. Trends Biotechnol. 2008; 26:14–20. [PubMed: 18037179]
13. Szostak JW, Bartel DP, Luisi PL. Synthesizing life. Nature. 2001; 409:387–390. [PubMed: 11201752]
14. Hu CMJ, Fang RH, Luk BT, Zhang L. Nanoparticle-detained toxins for safe and effective vaccination. Nat Nanotechnol. 2013; 8:933–938. [PubMed: 24292514]
15. Hu CMJ, et al. Nanoparticle biointerfacing by platelet membrane cloaking. Nature. 2015; 526:118–121. [PubMed: 26374997]
16. Brown AC, et al. Ultrasoft microgels displaying emergent platelet-like behaviours. Nat Mater. 2014; 13:1108–1114. [PubMed: 25194701]
17. Hu Q, et al. Engineered nanoplatelets for enhanced treatment of multiple myeloma and thrombus. Adv Mater. 2016; 28:9573–9580. [PubMed: 27626769]
18. Molinaro R, et al. Biomimetic proteolipid vesicles for targeting inflamed tissues. Nat Mater. 2016; 15:1037–1046. [PubMed: 27213956]
19. Boyer C, Zasadzinski JA. Multiple lipid compartments slow vesicle contents release in lipases and serum. ACS Nano. 2007; 1:176–182. [PubMed: 18797512]
20. Wong B, et al. Design and in situ characterization of lipid containers with enhanced drug retention. Adv Mater. 2011; 23:2320–2325. [PubMed: 21608043]
21. Marguet M, Edembe L, Lecommandoux S. Polymersomes in polymersomes: multiple loading and permeability control. Angew Chem Int Ed Engl. 2012; 51:1173–1176. [PubMed: 22190263]
22. Peters RJRW, et al. Cascade reactions in multicompartmentalized polymersomes. Angew Chem Int Ed Engl. 2014; 53:146–150. [PubMed: 24254810]
23. Elani Y, Law RV, Ces O. Vesicle-based artificial cells as chemical microreactors with spatially segregated reaction pathways. Nat Commun. 2014; 5:5305–5309. [PubMed: 25351716]
24. Chiu HC, Lin YW, Huang YF, Chuang CK, Chern CS. Polymer vesicles containing small vesicles within interior aqueous compartments and pH-responsive transmembrane channels. Angew Chem Int Ed Engl. 2008; 47:1875–1878. [PubMed: 18176922]
25. Lu Y, Aimetti AA, Langer R, Gu Z. Bioresponsive materials. Nat Rev Mater. 2016; 2:16075.
26. Hata Y, Slaughter CA, Südhof TC. Synaptic vesicle fusion complex contains unc-18 homologue bound to syntaxin. Nature. 1993; 366:347–351. [PubMed: 8247129]
27. Kaiser CA, Schekman R. Distinct sets of SEC genes govern transport vesicle formation and fusion early in the secretory pathway. Cell. 1990; 61:723–733. [PubMed: 2188733]
28. Söllner T, et al. SNAP receptors implicated in vesicle targeting and fusion. Nature. 1993; 362:318–324. [PubMed: 8455717]
29. Marsden HR, Tomatsu I, Kros A. Model systems for membrane fusion. Chem Soc Rev. 2011; 40:1572–1585. [PubMed: 21152599]
30. Lygina AS, Meyenberg K, Jahn R, Diederichsen U. Transmembrane domain peptide/peptide nucleic acid hybrid as a model of a SNARE protein in vesicle fusion. Angew Chem Int Ed Engl. 2011; 50:8597–8601. [PubMed: 21786370]
31. Robson Marsden H, Elbers NA, Bomans PHH, Sommerdijk NAJM, Kros A. A reduced SNARE model for membrane fusion. Angew Chem Int Ed Engl. 2009; 48:2330–2333. [PubMed: 19222065]
32. Meyenberg K, Lygina AS, van den Bogaart G, Jahn R, Diederichsen U. SNARE derived peptide mimic inducing membrane fusion. Chem Commun (Camb). 2011; 47:9405–9407. [PubMed: 21773636]
33. Tomatsu I, et al. Influence of pegylation on peptide-mediated liposome fusion. J Mater Chem. 2011; 21:18927–18933.

34. Kong L, Askes SHC, Bonnet S, Kros A, Campbell F. Temporal control of membrane fusion through photolabile PEGylation of liposome membranes. Angew Chem Int Ed Engl. 2016; 55:1396–1400. [PubMed: 26661729]
35. Gong Y, Ma M, Luo Y, Bong D. Functional determinants of a synthetic vesicle fusion system. J Am Chem Soc. 2008; 130:6196–6205. [PubMed: 18402445]
36. Chan YHM, van Lengerich B, Boxer SG. Effects of linker sequences on vesicle fusion mediated by lipid-anchored DNA oligonucleotides. Proc Natl Acad Sci USA. 2009; 106:979–984. [PubMed: 19164559]
37. Steinmetz MO, et al. Molecular basis of coiled-coil formation. Proc Natl Acad Sci USA. 2007; 104:7062–7067. [PubMed: 17438295]
38. Mo R, Jiang T, Gu Z. Enhanced anticancer efficacy by ATP-mediated liposomal drug delivery. Angew Chem Int Ed Engl. 2014; 53:5815–5820. [PubMed: 24764317]
39. Zhao C, Qu K, Ren J, Qu X. Proton-fueled DNA-duplex-based stimuli-responsive reversible assembly of single-walled carbon nanotubes. Chemistry. 2011; 17:7013–7019. [PubMed: 21542040]
40. Li X, Peng Y, Ren J, Qu X. Carboxyl-modified single-walled carbon nanotubes selectively induce human telomeric i-motif formation. Proc Natl Acad Sci USA. 2006; 103:19658–19663. [PubMed: 17167055]
41. Kisak ET, Coldren B, Zasadzinski JA. Nanocompartments enclosing vesicles, colloids, and macromolecules via interdigitated lipid bilayers. Langmuir. 2002; 18:284–288.
42. Tunuguntla RH, Allen FI, Kim K, Belliveau A, Noy A. Ultrafast proton transport in sub-1-nm diameter carbon nanotube porins. Nat Nanotechnol. 2016; 11:639–644. [PubMed: 27043198]
43. Efrat S. Making sense of glucose sensing. Nat Genet. 1997; 17:249–250. [PubMed: 9354775]
44. Matsumoto R, et al. A liposome-based energy conversion system for accelerating the multi-enzyme reactions. Phys Chem Chem Phys. 2010; 12:13904–13906. [PubMed: 20848047]
45. Wang Z, Thurmond DC. Mechanisms of biphasic insulin-granule exocytosis: roles of the cytoskeleton, small GTPases and SNARE proteins. J Cell Sci. 2009; 122:893–903. [PubMed: 19295123]
46. Schuette CG, et al. Determinants of liposome fusion mediated by synaptic SNARE proteins. Proc Natl Acad Sci USA. 2004; 101:2858–2863. [PubMed: 14981239]
47. Mo R, Jiang T, Di J, Tai W, Gu Z. Emerging micro- and nanotechnology based synthetic approaches for insulin delivery. Chem Soc Rev. 2014; 43:3595–3629. [PubMed: 24626293]
48. Kitabchi AE, Umpierrez GE, Miles JM, Fisher JN. Hyperglycemic crises in adult patients with diabetes. Diabetes Care. 2009; 32:1335–1343. [PubMed: 19564476]
49. Park MH, Joo MK, Choi BG, Jeong B. Biodegradable thermogels. Acc Chem Res. 2012; 45:424–433. [PubMed: 21992012]
50. Ye H, Daoud-El Baba M, Peng RW, Fussenegger M. A synthetic optogenetic transcription device enhances blood-glucose homeostasis in mice. Science. 2011; 332:1565–1568. [PubMed: 21700876]
51. Peppas NA, Khademhosseini A. Make better, safer biomaterials. Nature. 2016; 540:335–338. [PubMed: 27974790]
52. Bakh NA, et al. Glucose-responsive insulin by molecular and physical design. Nat Chem. 2017; 9:937–943. [PubMed: 28937662]
53. Boni LT, et al. Curvature dependent induction of the interdigitated gel phase in DPPC vesicles. Biochim Biophys Acta. 1993; 1146:247–257. [PubMed: 8452859]
54. Ahl PL, et al. Interdigitation-fusion: a new method for producing lipid vesicles of high internal volume. Biochim Biophys Acta. 1994; 1195:237–244. [PubMed: 7947916]
55. Kasahara M, Hinkle PC. Reconstitution of D-glucose transport catalyzed by a protein fraction from human erythrocytes in sonicated liposomes. Proc Natl Acad Sci USA. 1976; 73:396–400. [PubMed: 1061142]
56. Kano K, Fendler JH. Pyranine as a sensitive pH probe for liposome interiors and surfaces. pH gradients across phospholipid vesicles. Biochim Biophys Acta. 1978; 509:289–299. [PubMed: 26400]

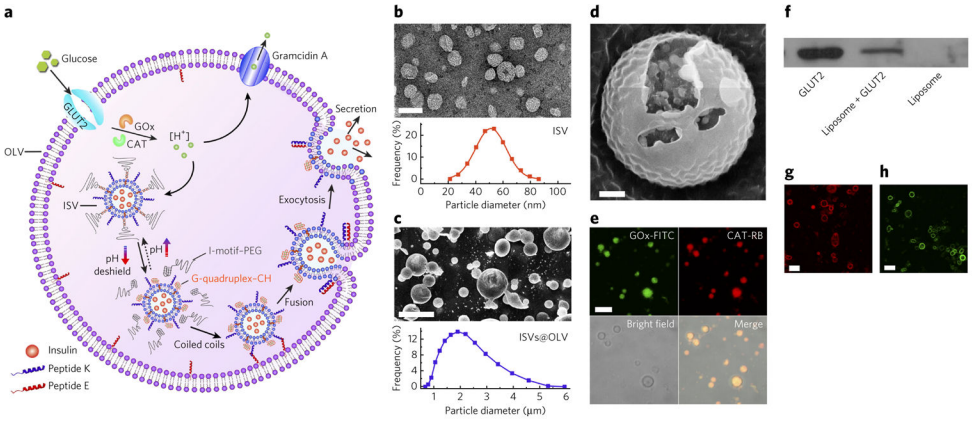

Figure 1. Design and synthesis of AβCs

(**a**) Schematic of the biochemical processes inside the AβCs. GOx, glucose oxidase; CAT, catalase; square brackets denote concentration. (**b**) Top, ISVs stained with uranyl acetate and imaged by TEM. The ISVs were used to mimic the insulin granules inside natural beta cells (scale bar, 100 nm). Bottom, size-distribution histogram of the insulin-containing ISVs. (**c**) Top, cryo-SEM micrograph of the vesicles-in-vesicle superstructures (scale bar, 5 μm). Bottom, size distribution of vesicles-in-vesicle superstructures (ISVs@OLV). (**d**) Magnified fractured cryo-SEM micrograph of the vesicles-in-vesicle superstructures (scale bar, 200 nm). From the fracture in d, small liposomal vesicles can be clearly seen inside the large liposome. (**e**) CLSM micrographs verifying the encapsulation of glucose oxidase labeled with fluorescein isothiocyanate (GOx-FITC) and catalase labeled with rhodamine B (CAT-RB) inside the large liposomes (scale bar, 5 μm). (**f**) Western blotting results indicating the retention of immunoreactivity of GLUT2 in the superstructures. The full gel is shown in Supplementary Figure 9. (**g**) CLSM image showing the reconstitution of GLUT2 labeled with rhodamine B on the membranes of the larger liposomes (scale bar, 5 μm). (**h**) CLSM image showing insertion of the proton channel gramicidin A labeled with lysine-5-carboxyfluorescein into the outer membrane (scale bar, 5 μm).

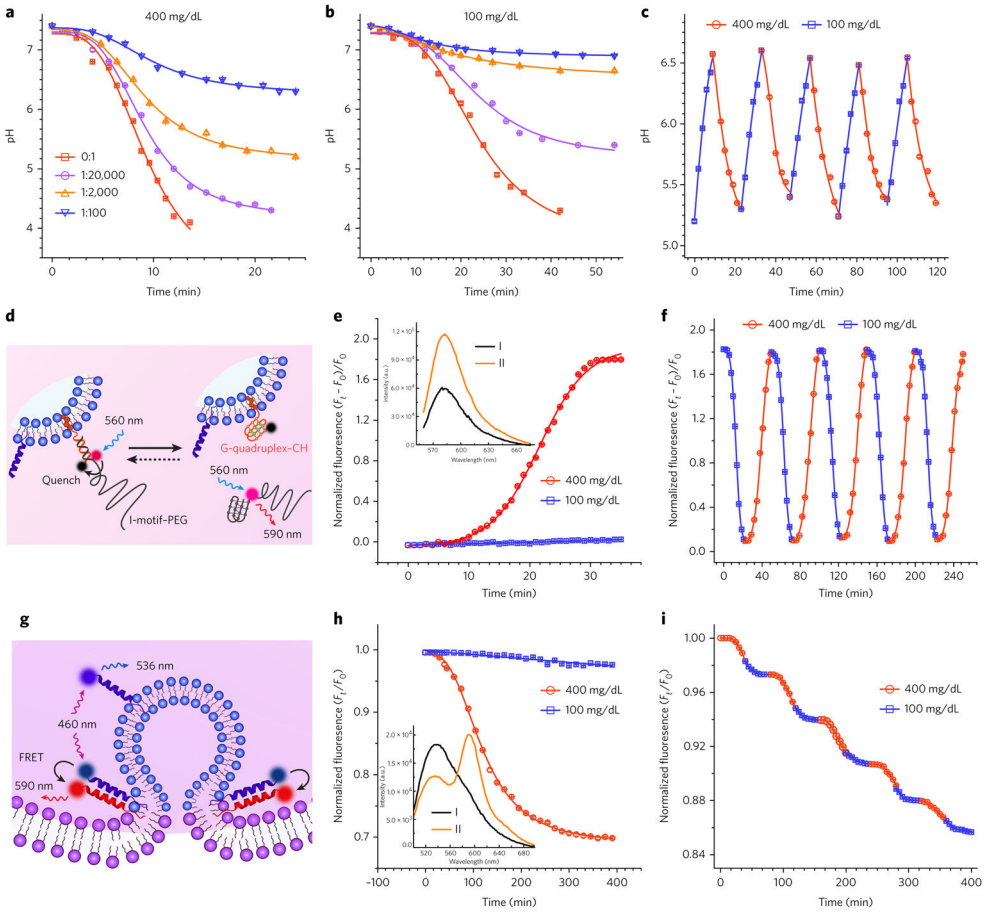

Figure 2. Biochemical processes inside AβCs

(**a–c**) Glucose-sensing ability of AβCs. pH variation inside AβCs in 400 mg/dL (**a**) and 100 mg/dL (**b**) glucose solutions. The ratios represent the relative amount of gramicidin A to that of dipalmitoylphosphatidylcholine lipid. (**c**) Reversible pH variation induced by alternatively switching environmental glucose concentrations. (**d–i**) Signal transduction inside AβCs to control PEG deshielding and peptide assembly. (**d**) Schematic for reversible PEG association and disassociation tuned by glucose metabolism. PEG–CDNA was labeled with the DNA donor tetramethylrhodamine (pink), and GDNA–CH was labeled with the DNA acceptor IAbRQ (black). (**e**) FRET assay showing dehybridization of the pH-sensitive DNA duplex that bridges the PEG shield and the ISV surface at different glucose concentrations. (**f**) Reversible quenching and recovery of the fluorescence of the DNA donor, demonstrating the reversible attachment and detachment of the PEG shield in high and low glucose solutions. (**g**) Schematic illustration of the quenching of the peptide donor nitrobenzofuran (blue) on peptide K by the peptide acceptor tetramethylrhodamine (red) on peptide E induced by peptide assembly after PEG dissociation. (**h**) FRET assay showing the interactions between peptide E and peptide K at different glucose concentrations. In **e** and **h**, F_0 and Ft represent the fluorescence intensity (in arbitrary units (a.u.)) measured before and at time t after addition into glucose solutions. In inset, I and II show the fluorescence spectra of the AβCs before and after incubation, respectively, in 400 mg/dL glucose solution. (**i**) Stepwise

decrease in the fluorescence intensity of the peptide donor after alternation of the glucose concentrations. Error bars, s.d. of three independent experiments ($n = 3$).

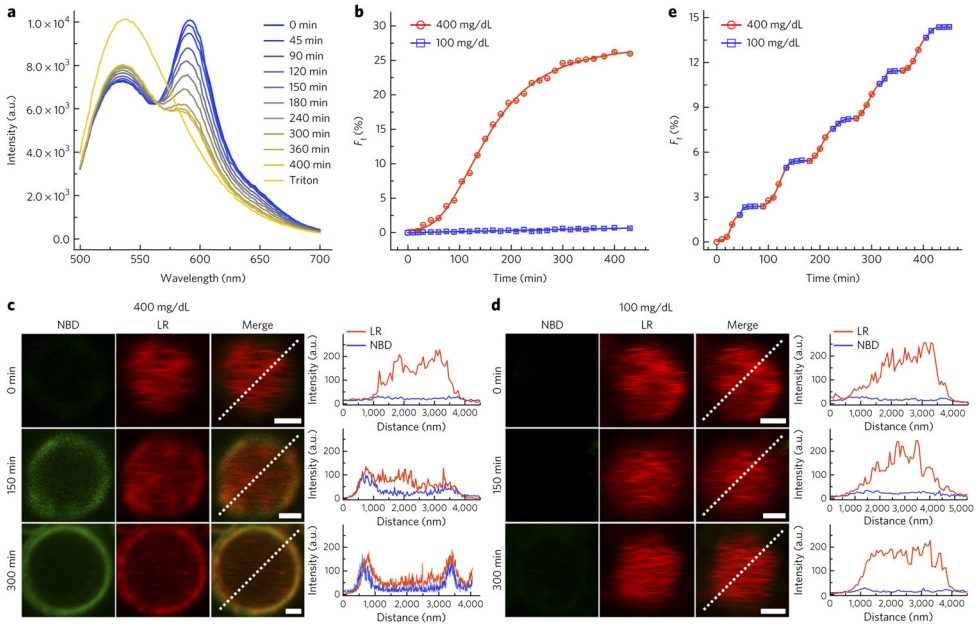

Figure 3. Membrane fusion of ISVs and OLVs after glucose metabolism

(**a**) Fluorescence spectra of AβCs after incubation in 400 mg/dL glucose solution for the indicated times. The ISVs were simultaneously labeled with lipid donor (NBD, emission λ_{max} = 536 nm) and lipid acceptor (LR, emission λ_{max} = 592 nm). The total lipid-donor fluorescence spectrum was obtained by disruption of AβCs with 1% Triton X-100. (**b**) Kinetics profiles of lipid mixing between lipid-donor- and lipid-acceptor-labeled ISVs and OLVs in 400 mg/dL and 100 mg/dl glucose solutions, as indicated by the increase in lipid-donor emission. Each data point represents an average of triplicate measurements with standard error <10%. (**c,d**) CLSM images showing lipid mixing between lipid-donor- and lipid-acceptor-labeled ISVs and OLVs in 400 mg/dL (**c**) and 100 mg/dL (**d**) glucose solutions after different incubation times (scale bars, 1 μm). The profiles show the distribution of the fluorescence intensity of lipid donor (green lines) and lipid acceptor (red lines) along the indicated white dashed lines. (**e**) Stepwise increase in the fluorescence of lipid donor after alternation of the glucose concentrations between 400 and 100 mg/dL. Error bars, s.d. of three independent experiments.

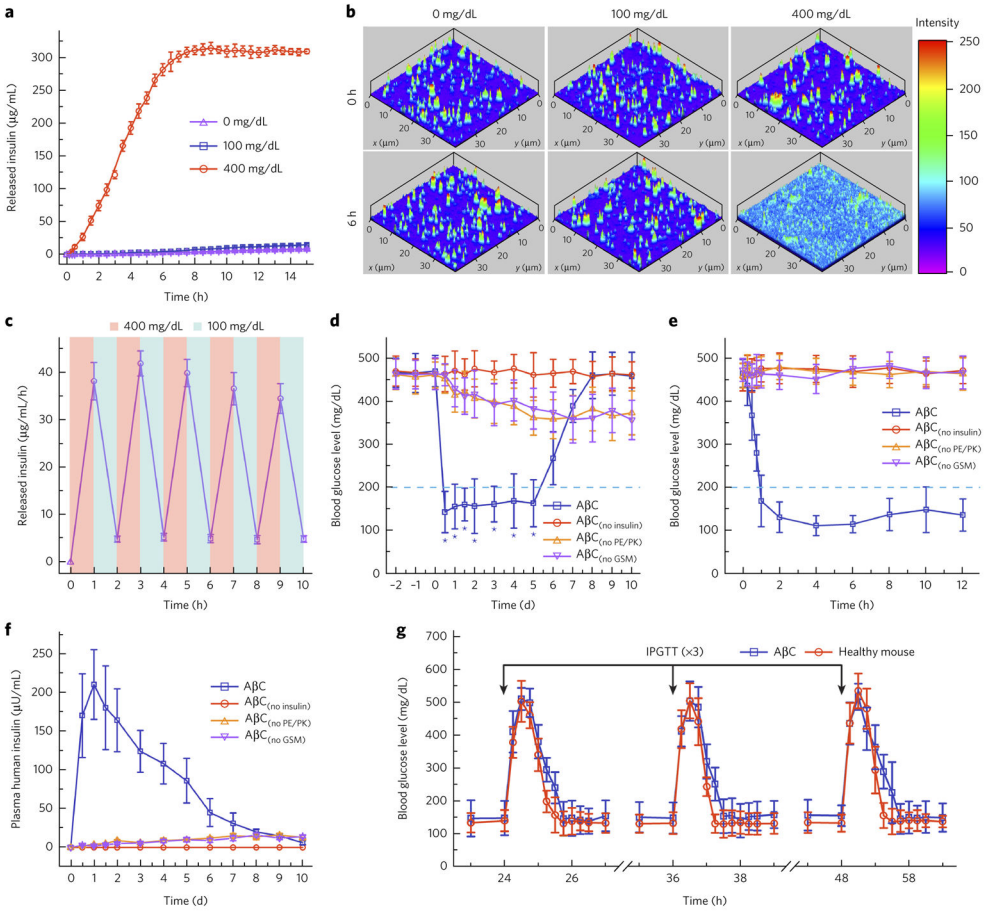

Figure 4. *In vitro* insulin secretion from AβCs and *in vivo* type 1 diabetes treatment

(**a**) *In vitro* accumulated-insulin release from AβCs incubated in solutions with different glucose concentrations. Data points represent mean ± s.d. (three independent experiments per group). (**b**) 2.5D CLSM images showing the fluorescence intensity and distribution of fluorescein labeled-insulin from AβCs before and after incubation in solutions containing different concentrations of glucose. (**c**) Pulsatile release profile by AβCs, showing the insulin release rate after alternation of the glucose concentration between 400 and 100 mg/dL. Data points represent mean ± s.d. ($n = 3$). (**d**) Blood glucose levels of diabetic mice after treatment with AβCs or control AβCs lacking insulin ($AβC_{(no\ insulin)}$), membrane-fusion peptide E and peptide K ($AβC_{(no\ PE/PK)}$) or glucose-sensing machinery ($AβC_{(no\ GSM)}$). Data points represent mean ± s.d. ($n = 5$ mice per group). $^*P < 0.001$ (analyzed by one-way ANOVA) for AβCs compared with control AβCs. (**e**) The blood glucose levels were continuously monitored in the first 12 h shown in d. Data points represent mean ± s.d. ($n = 5$ mice per group). (**f**) Variation in plasma insulin concentrations in diabetic mice over time after injection of AβC or control AβCs. Data points represent mean ± s.d. ($n = 5$ mice per group). (**g**) *In vivo* intraperitoneal glucose tolerance test (IPGTT) performed on diabetic mice at 24, 36 and 48 h after AβC treatment and on healthy control mice. Data points represent mean ± s.d. ($n = 5$ mice per group).